Membrane-immobilized transaminases for enantiopure amines synthesis

Hippolyte Meersseman Arango,[a] Xuan Dieu Linh Nguyen,[a] Patricia Luis,[b] Tom Leyssens,[a] David Roura Padrosa,[c] Francesca Paradisi,[c] Damien P. Debecker[a,*]

[a] Institute of Condensed Matter and Nanosciences (IMCN), Université catholique de Louvain (UCLouvain), Place Louis Pasteur, 1, 1348 Louvain-La-Neuve, Belgium

[b] Materials & Process Engineering (iMMC-IMAP), Université catholique de Louvain, Place Sainte Barbe 2, 1348 Louvain-la-Neuve, Belgium

[c] Department of Chemistry and Biochemistry, University of Bern, Freiestrasse 3, Bern, Switzerland

* damien.debecker@uclouvain.be

Supplementary material

1 Experimental details - Characterization of the membrane carriers and of the biocatalytic membranes

Attenuated Total Reflectance - InfraRed Spectroscopy (ATR-FTIR)

The presence of functional groups at the PAN and PP (pristine and functionalized) membrane surfaces was investigated by Attenuated Total Reflectance - InfraRed Spectroscopy (ATR-FTIR). Membrane surfaces were analyzed using a Bruker Equinox 55 with a Platinum ATR cell, with a diamond crystal, and Trans DTGS detector. 100 scans were taken for both background and samples, with a resolution of 2 cm^{-1}. ATR correction was applied (number of ATR reflection is 1; angle of incidence is 45°; mean reflection index of sample is 1.5).

X-ray Photoelectron Spectroscopy (XPS)

Elemental surface compositions of PAN and PP (pristine and functionalized) membranes were assessed *via* X-ray photoelectron spectroscopy (XPS). XPS analyses were carried out in a SSX 100/206 photoelectron spectrometer from Surface Science Instruments (USA) equipped with a monochromatized micro focused Al X-ray source (powered at 20 mA and 10 kV). The pressure in the analysis chamber was around 10^{-6} Pa and the flood gun was set at 8 eV. The angle between the surface and the axis of the analyzer lens was 55◦. The analyzed area was approximately 1.4 mm^2 and the pass energy was set at 150 eV. Under these conditions, the full width measured at half maximum (FWHM) of the Au 4f7/2 peak for a clean gold standard sample was about 1.6 eV. Samples were prepared as 1x1 cm^2 squares and were fixed by using a piece of double-sided insulating tape, and placed on a ceramic carousel with a Ni grid set above the sample surface for charge stabilization. The following sequence of spectra was recorded: survey spectrum, C 1s, O 1s, N 1s, Na 1s, F 1s, and C 1s again to check the stability of charge compensation with time. The C-(C,H) component of the C1s peak of carbon was fixed at 284.8 eV to calibrate the binding energy scale. Data treatment was performed with the CasaXPS program (Casa Software Ltd, UK). Carbon 1s peaks were decomposed with the least squares fitting routine provided by the software with a Gaussian/Lorentzian (85/15) product function and after subtraction of a non-linear baseline.

Water contact angle (WCA)

The hydrophobicity/hydrophilicity nature of the membranes was evaluated using the optical water contact angle (WCA) (DataPhysics OCA20). Three measurements were taken for each membrane sample using a sessile drop method with a 5 μL droplet of water.

Scanning electron microscopy (SEM)

The morphology and porosity of the membrane carriers were analyzed by performing Scanning Electron Microscopy (SEM) images (Ultra 55 Feg Sem, Zeiss, Zaventem, Belgium). The membranes cross-section were also observed. Prior to the SEM analysis, membranes were beforehand immersed into liquid nitrogen for a clean cross-sectional cut, and a thin layer of gold was deposited under vacuum with a sputter coater (Quorum Q150 RS) to make the samples conductive.

Soluble enzymes quantification : Bradford method

Soluble enzyme concentrations were assessed through the Bradford titration method [1]. Calibration was performed by mixing 250 µL of standard solutions of TA cell-free extracts in HEPES 0.1M buffer pH 8, sodium pyruvate 10 mM, PLP 1 mM (within 0–0.16 $mg.mL^{-1}$ concentration range) with 750 µL of Bradford reagent. After 5 minutes incubation at room temperature, absorbances were read at 595 nm with a ThermoScientific Genesys 10S-Vis spectrophotometer, and values of A_{595} were plotted against TA concentration.

Immobilized PLP loading evaluation

When co-immobilization of TA and PLP was attempted, the amount of PLP loaded onto the membrane was determined by measuring the absorbance at 390 nm of 1 mL solutions using a ThermoScientific Genesys 10S-Vis spectrophotometer. Calibration curve was performed using standard solutions of HEPES 0.1M buffer pH 8, sodium pyruvate 10 mM containing different PLP concentrations (within 0–0.5 mM concentration range). The PLP immobilization yield (Y_{PLP}) was computed using Eq. (a), where $[PLP]_0$, $[PLP]_1$ and $[PLP]_{Ri}$ stand for the PLP concentration in the immobilization (i.e. 0.1 mM or 1 mM for TA immobilization, 1 mM for PLP immobilization), residual and rinsing solutions, respectively.

$$L_{PLP} = 5 \times \left([PLP]_0 - [PLP]_1 - \Sigma[PLP]_{Ri}\right) \ [\mu mol] \#Eq.(a)$$

Gas Chromatography (GC) analysis

After extraction of the analytes into dichloromethane, the analysis was performed on a Bruker Scion 456-GC with a WCOT fused silica BR-5 column (30 m x 0.32 mm ID x 1.0 µm) and helium as carrier gas (25 $mL.min^{-1}$), oven temperature at 150 °C, split ratio of 80, injector

temperature at 250 °C, flame ionization detector temperature at 300 °C (air flow 300 mL.min^{-1}, H_2 flow 30 mL.min^{-1}).

Chiral High Performance Liquid Chromatography (cHPLC) analysis

R and S enantiomers of bromo-α-methylbenzylamine were detected by normal phase HPLC (Hitachi-koki, Chiyoda, Japan) at 252 nm using a Merck-Hitachi LaChrom L-7000 HPLC and a Chiralpak AD-H (250 mm × 4.6 mm) column with a flow rate of 1 mL/min (95% isohexane/5% 2-propanol/0.1% diethylamine) for 30 min. The retention times of the S- and R-enantiomers were 4.79 and 6.30 min, respectively.

2 Supplementary data (Figures, Table, and remarks)

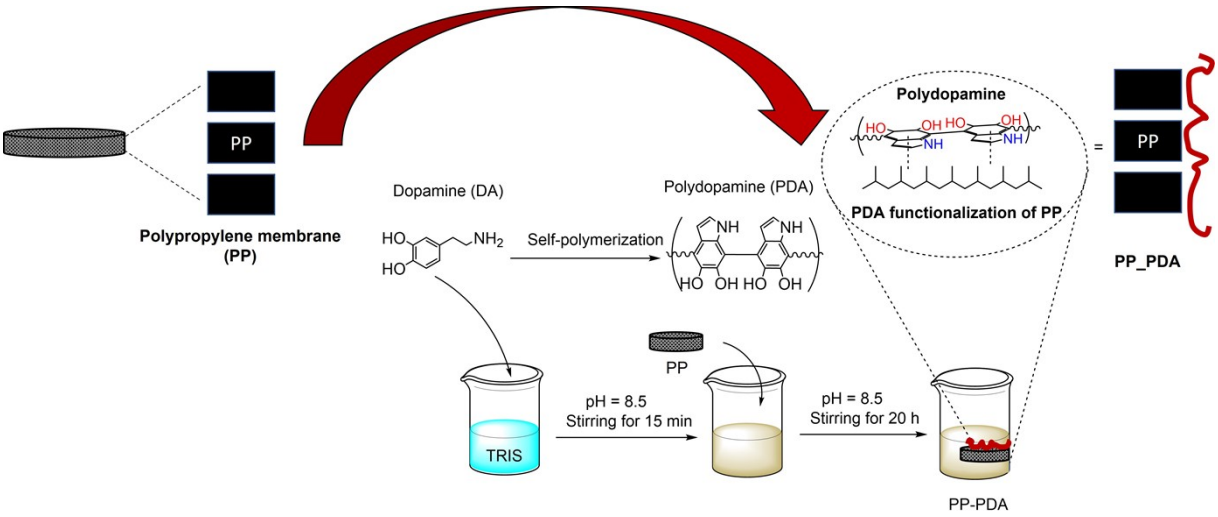

Figure S1. Schematic representation of the PDA deposition on PP membrane surface, reproduced from [2].

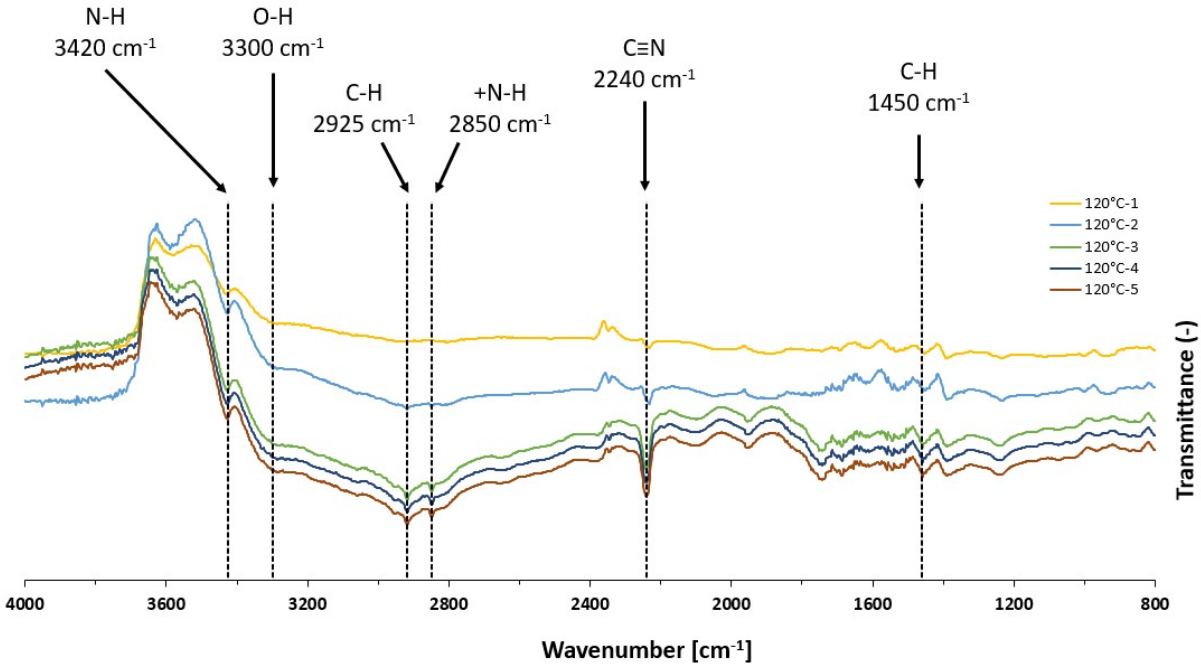

Figure S2. Diffuse reflectance infrared Fourier transform spectroscopy (DRIFTS) spectra (in transmittance) obtained on the HPAN_PEI1 heated at 120 °C (under air). Each series on the graph (i.e. each line) represents a run of analysis. Each run was performed every two minutes.

Table S1. Main bond vibrations wavenumbers (in cm^{-1}) of the different species of interest (i.e. amines, amides, carboxylic acids, alkanes, amides and nitriles)

Bond vibration mode	**Amines**		
	I	**II**	**III**
H-N-H scissors	1600-1650	/	/
N-CH_3 and N-$(CH_3)_2$ stretching	/	2780	2780 and 2850
N-H stretching	3300 and 3400	3300 (broad)	/
	Amine salts		
	I	**II**	**III**
+N-H bending	1560-1630	1500-1530 and 1560-1630	/
+N-H stretching	2800-3000	2800-3000	2300-2700
	Amides		
	I	**II**	
C-N stretching	1400	1250-1300	
C=O stretching	1650-1680	1650-1680	
N-H stretching	3150-3350	3150-3350	
	Carboxylic acids/carboxylates		
O-H stretching	2500-3300 (very broad and strong)		
C=O stretching	1730		
COO- stretching	1560		
O-H bending	1400		
	Alkanes		
C-H stretching	2925		
C-H bending	1450		
	Epoxides		
Ring stretching	1230-1280		
-C-O-C- stretching	810-950		
-C-O-C- stretching	750-880		
	Nitriles		
C≡N stretching	2240		

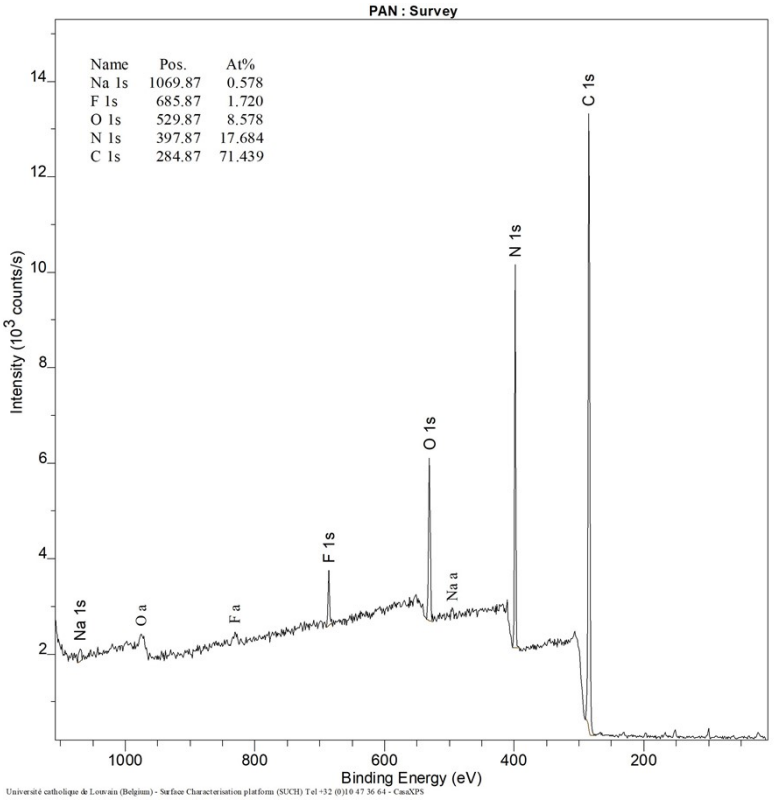

Figure S3. XPS spectrum of the pristine PAN membrane

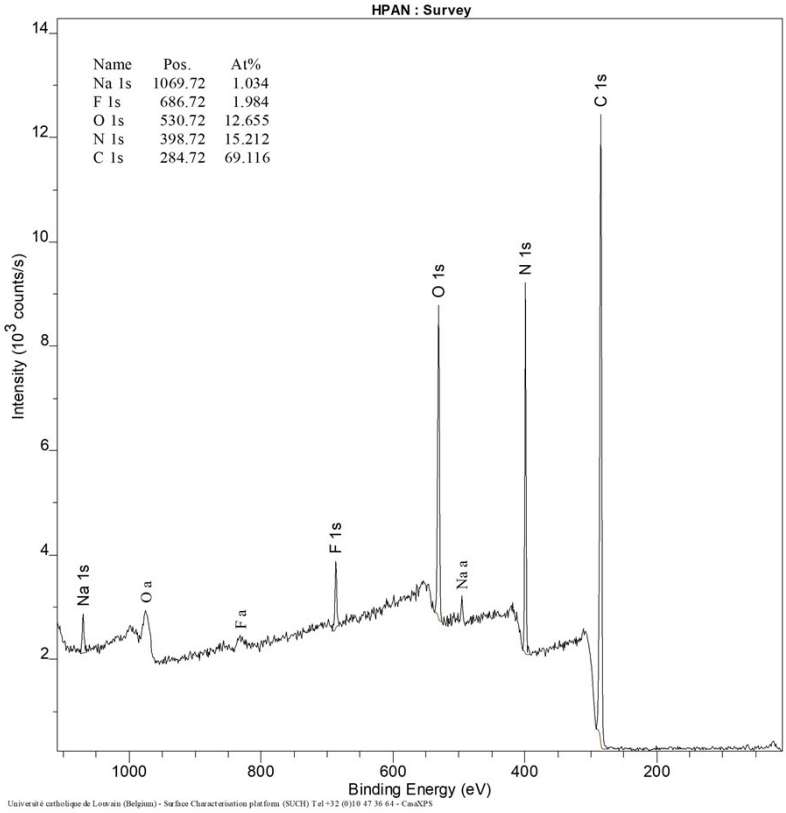

Figure S4. XPS spectrum of the HPAN membrane

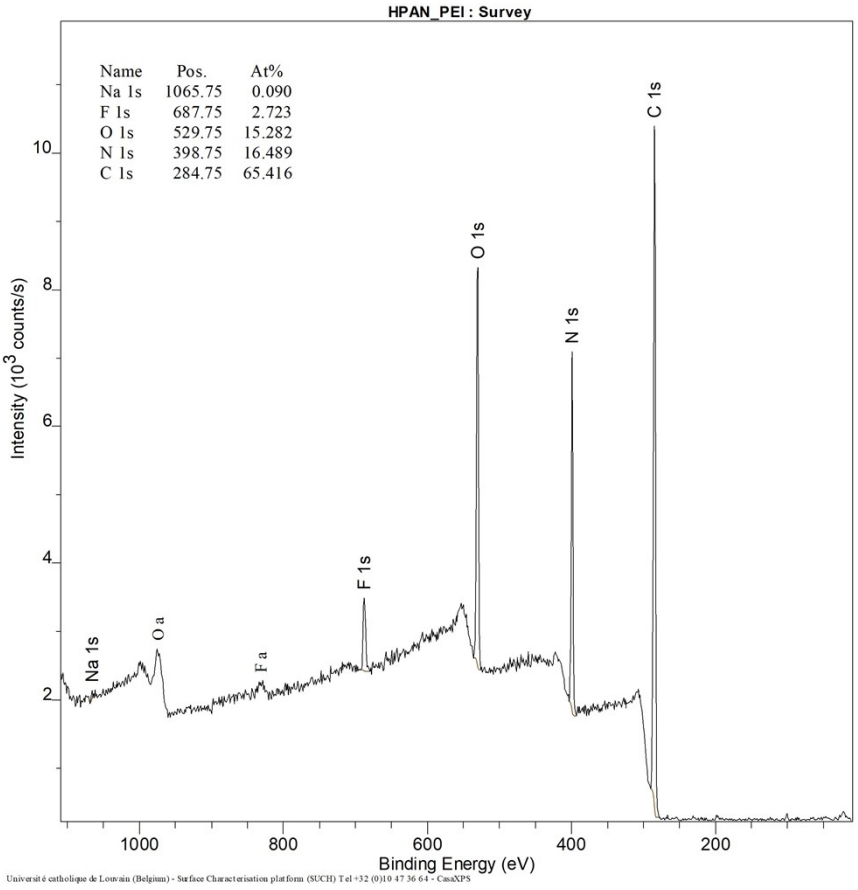

Figure S5. XPS spectrum of the HPAN_PEI1 membrane

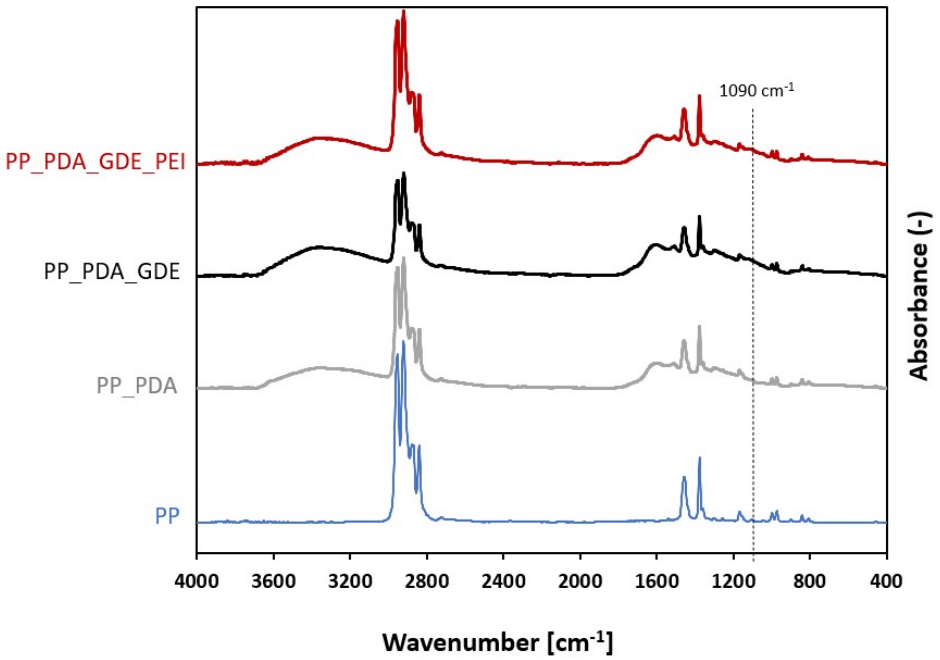

Figure S6. ATR-FTIR spectra of the pristine PP (blue), of PP_PDA (grey), PP_PDA_GDE (black) and of PP_PDA_GDE_PEI (red).

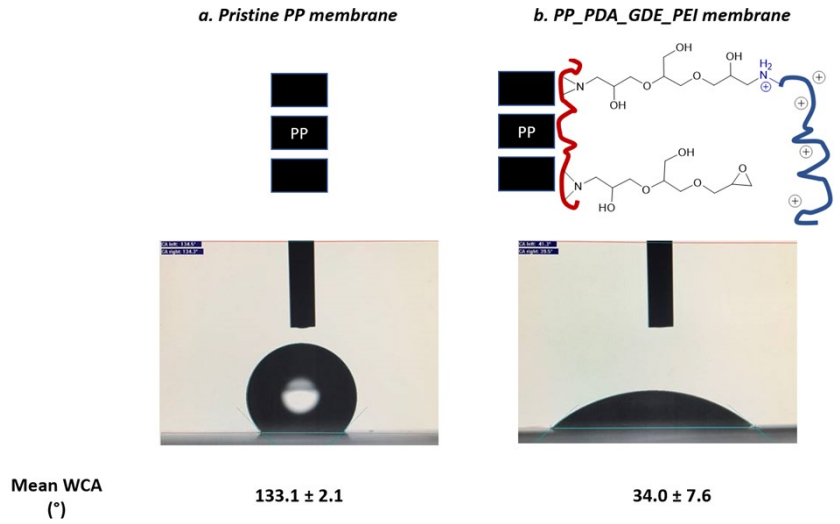

Figure S7. Schematic representation (top) and water contact angle (WCA) measurements (bottom) of **a)** pristine PP and **b)** PP_PDA_GDE_PEI membranes. Mean WCA represent the average values of the measurements taken at 5 different spots of c.a. 3 cm^2 membranes sheets.

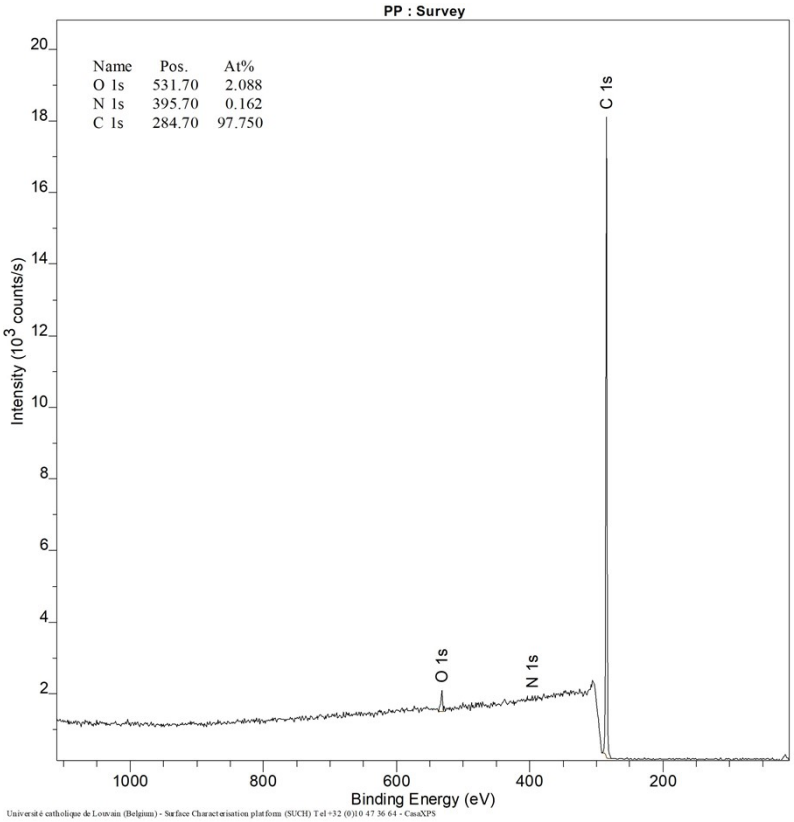

Figure S8. XPS spectrum of the pristine PP membrane

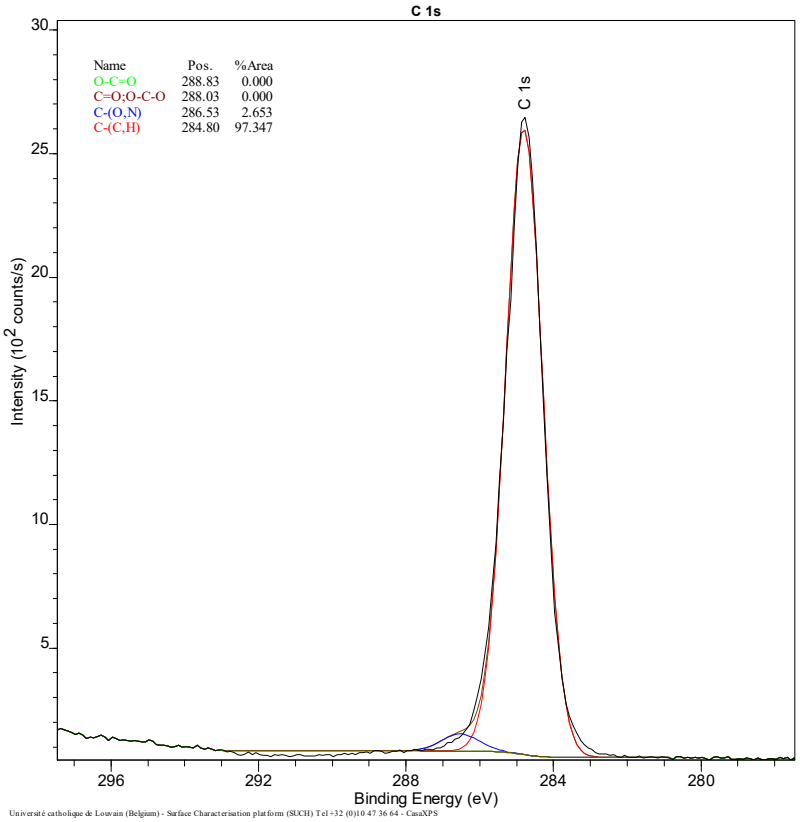

Figure S9. C1s peak deconvolution (resulting from the pristine PP membrane analysis by XPS)

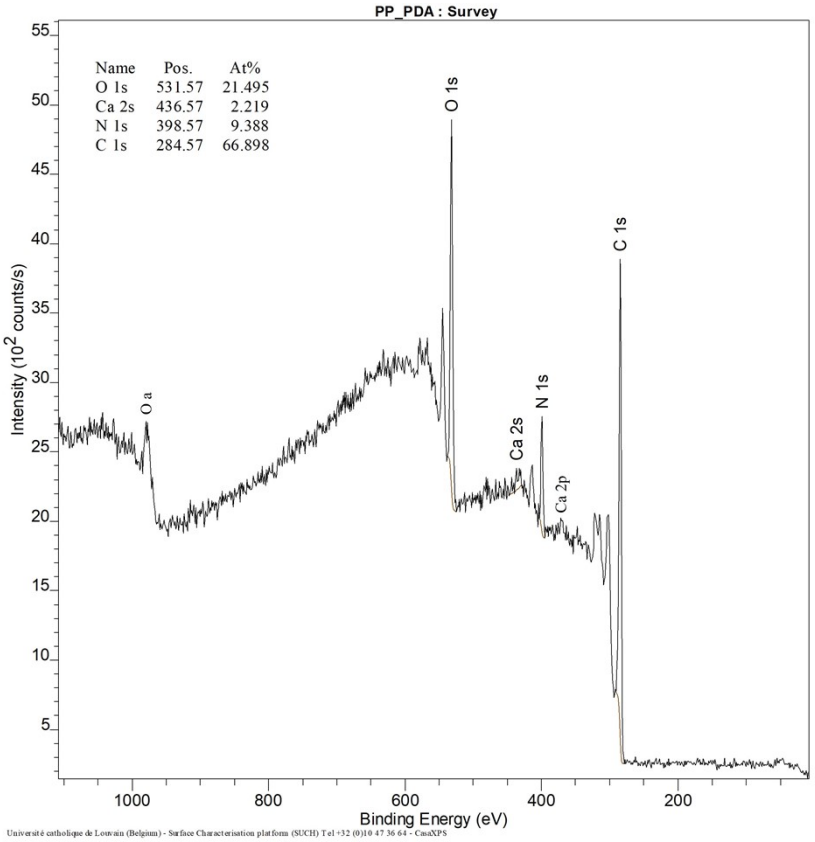

Figure S10. XPS spectrum of the PP_PDA membrane

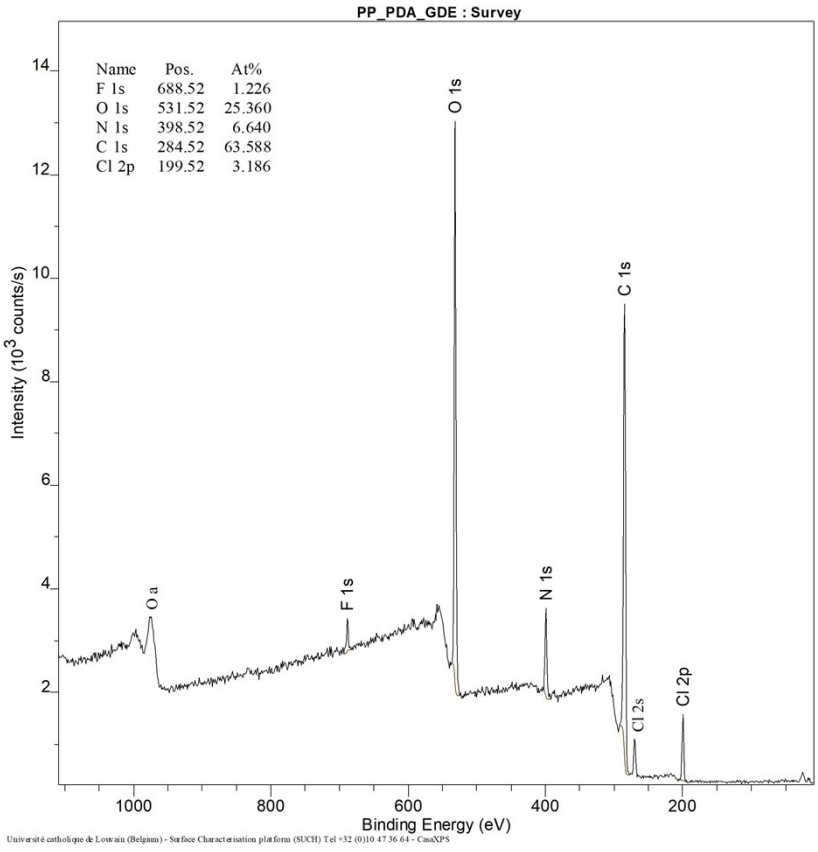

Figure S11. XPS spectrum of the PP_PDA_GDE membrane

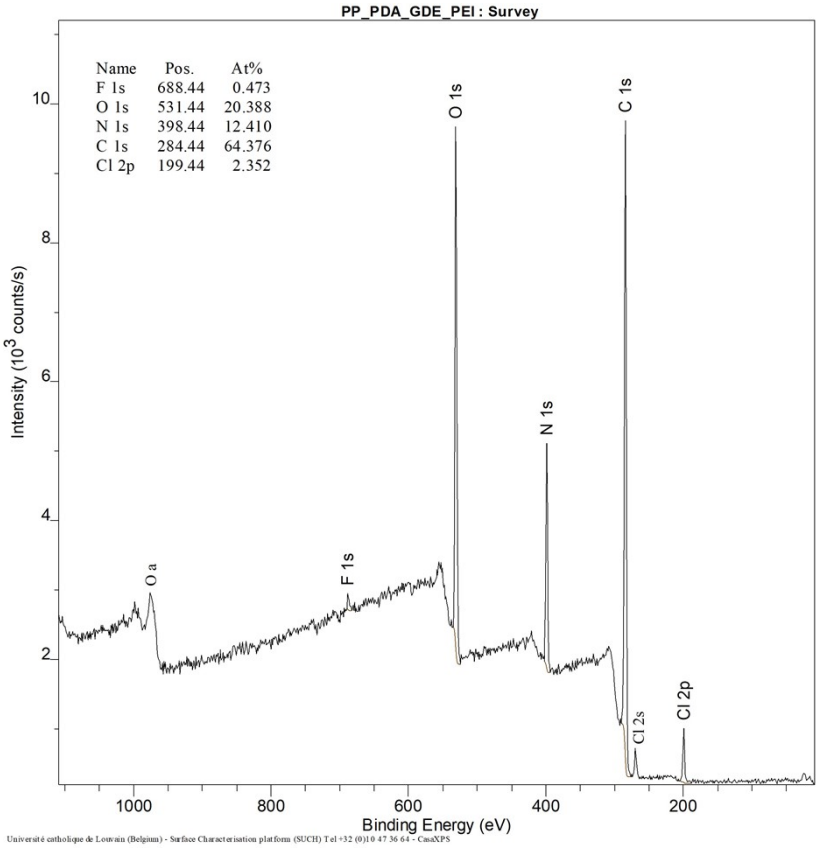

Figure S12. XPS spectrum of the PP_PDA_GDE_PEI membrane

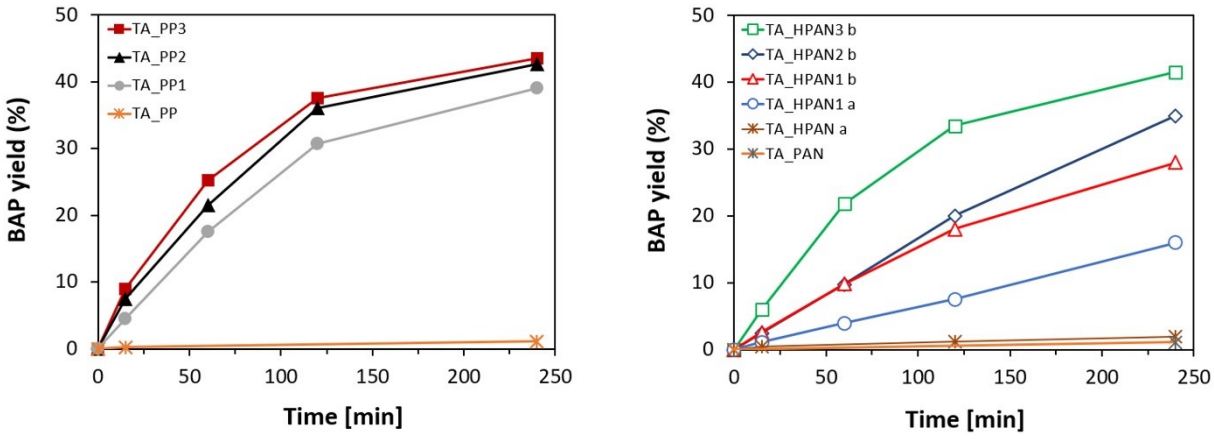

Figure S13. Activity profiles displayed by the different PP-immobilized (left) and PAN-immobilized (right) HeWT biocatalysts in the kinetic resolution of BMBA (using C_0 = 0.25 mg/mL TsRTA as immobilization concentration).

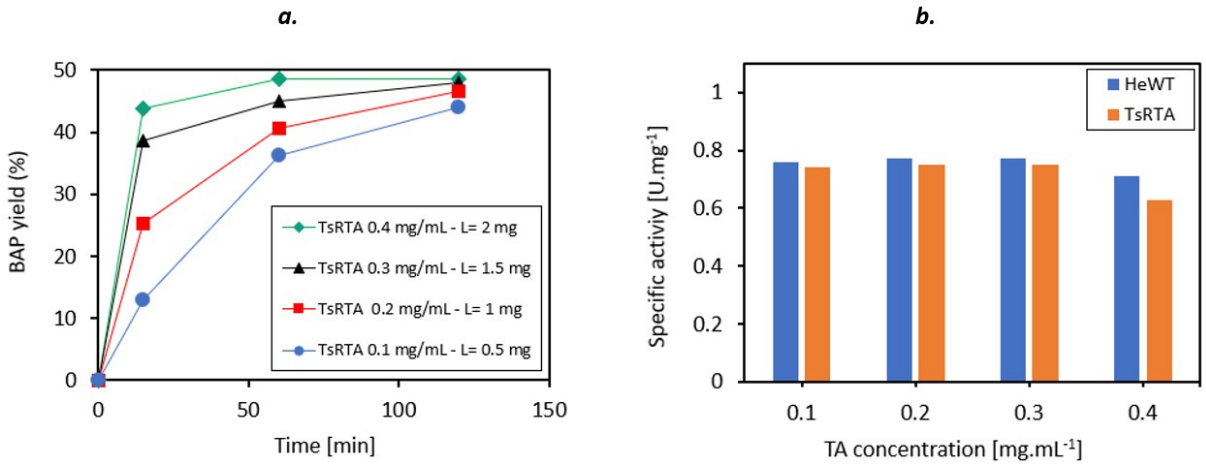

Figure S14. Activity profiles displayed by soluble TsRTA at different concentrations (in mg/mL) and corresponding enzyme content L (in mg) (left) and specific activity of the soluble TAs (HeWT in blue and TsRTA in orange) at different enzyme concentrations (right).

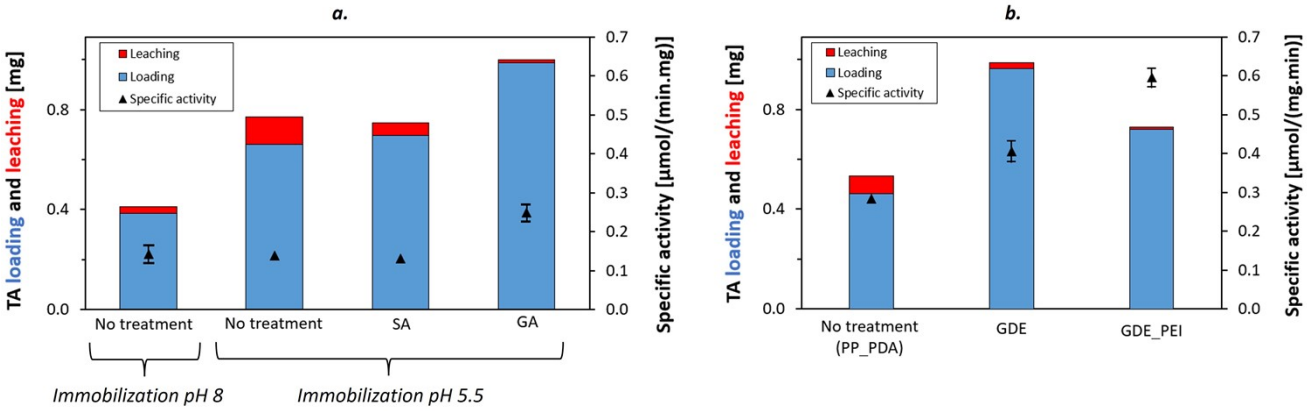

Figure S15. Immobilized TsRTA loading (blue) and leaching (red) (left axis), and specific activity (black triangles) (right axis) observed on **a)** different HPANx supports (from left to right : HPAN1a, HPAN1b, HPAN2b, HPAN3b) and **b)** PPy carriers (from left to right : PP1, PP2, PP3) and **b)** PP_PDA carriers, at constant immobilization concentration (C_0 = 0.25 mg/mL TsRTA). Error bars represent the standard deviations obtained on triplicates.

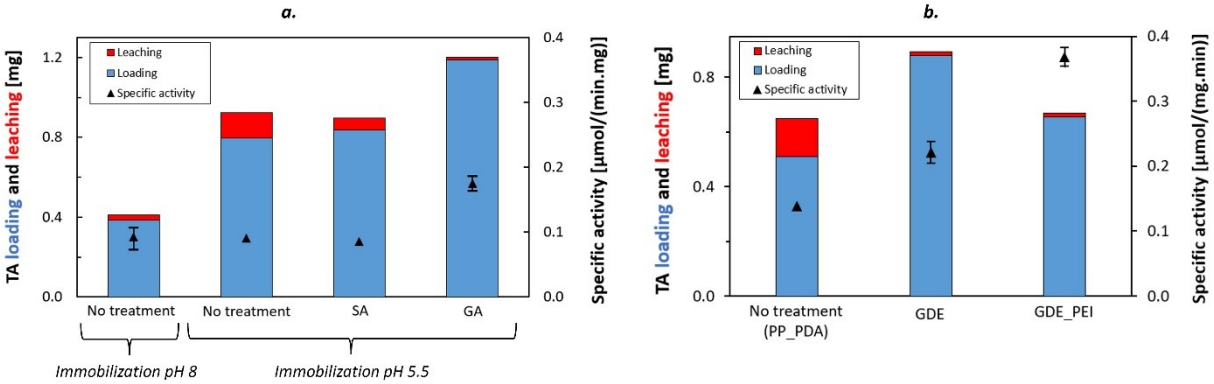

Figure S16. Immobilized HeWT loading (blue) and leaching (red) (left axis), and specific activity (black triangles) (right axis) observed on **a)** different HPANx supports (from left to right : HPAN1a, HPAN1b, HPAN2b, HPAN3b) and **b)** PPy carriers (from left to right : PP1, PP2, PP3), at constant immobilization concentration (C_0 = 0.25 mg/mL HeWT). Error bars represent the standard deviations obtained on triplicates.

Comparison of the catalytic performance with other immobilized TAs

In order to compare to compare the catalytic performance of different immobilized TAs, it is often useful to consider their specific activities (or specific activity recoveries, with respect to free enzymes) and immobilization yields (or immobilization efficiency). In this study, we employ small pieces of flat-sheet membranes (i.e. 5 cm^2, which corresponds to 25 mg and 40 mg of functionalized PP and PAN membranes, respectively) as support, hence the enzyme loadings achieved on our heterogeneous catalysts are limited. This issue could be easily overcome by linear scaling-up of the membrane, and employing more ideal membrane configurations (displaying higher interfacial area, e.g. industrial membrane modules) instead of simple flat-sheets.

As matter of comparison, our best-performing membrane-immobilized biocatalysts seem to perform better or similarly in terms of specific activity recovery and immobilization efficiency compared to a series of TAs immobilized on a variety of different supports (Table S2), including polycarvone acrylate di-epoxide (PCADE)-functionalized membranes, 2D-zeolites, functionalized lignin, functionalized epoxy-resin). Among the best results that can be found in the literature, Heckmann and Paradisi managed to obtain 170 mg_{TA}/g_{resin} (corresponding to 70% immobilization yield) displaying 38% of specific activity recovery, and 400 mg_{TA}/gr_{esin} with 62% specific activity recovery using *RTA-43 and HeWT_F48W, respectively [3].

Table S2: Comparison of the immobilization and catalytic performance of the membrane-immobilized TAs reported in this work (using an enzyme concentration of C_0 = 0.5 mg/mL for the TA immobilization), with other immobilized TAs.

Ref.	Immob. biocatalyst	Immob. yield (%)	Immob. Efficiency [$mg_{TA}.g_{carrier}^{-1}$]	Sp. acti recovery (%)
This work	TSRTA_PP3	42	48	71
	TsRTA_PP3_SS	78	88	41
	TsRTA_HPAN3b	62	40	23
Howdle et al. [4]	HeWT_PCADE	62	6.2	44
Corma et al. [5]	TA_zeolites2D	80	50	62
Paradisi et al. [6]	HeWT_lignin	100	5	19

Paradisi et al. [7]	HeWT_resin	100	1	31
Paradisi and Heckmann [3]	HeWT_F48W_resin	100	400	62
	*RTA-43_resin	70	170	38

2.1 Optimization of TA immobilization

2.1.1 TA on HPAN membranes

The best membrane functionalization and enzyme immobilization strategy (TsRTA_HPAN3b) was selected for further study, in an attempt to further boost catalytic performance of the resulting membranes. The effect of PEI concentration and GA post-treatment duration were screened (Figure S16). Functionalization with PEI did not affect markedly the enzyme loading, but a marked improvement of the specific activity of the immobilized TAs was observed from PEI concentrations of 0.5 wt.%. No further significant improvement could be achieved by further increasing the PEI concentration, which might indicate a saturation of this polyelectrolyte layer at the membrane surface. The TA leaching was always minor, whatever the PEI concentration, owing to the effective GA cross-linking. The effectiveness of this post-treatment with GA is similar whatever the duration (Figure S16b).

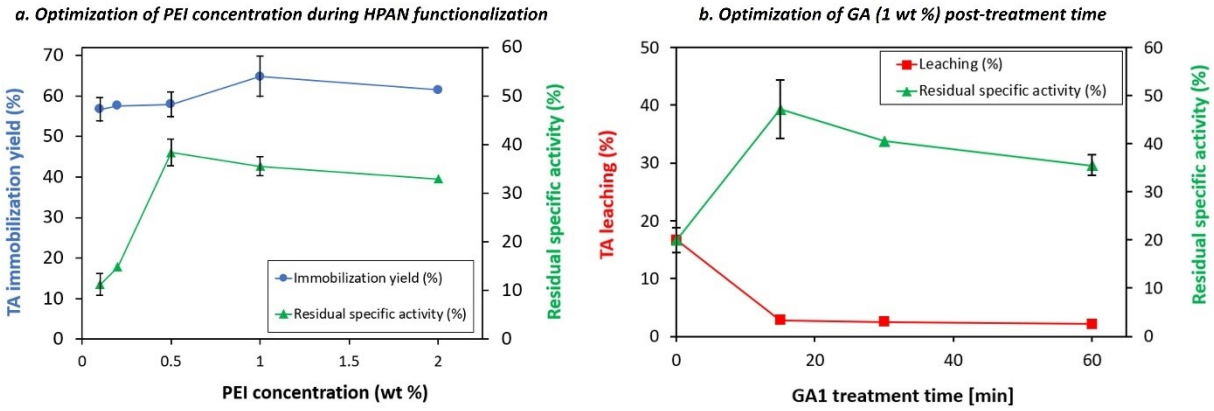

Figure S17. Impact of **a)** PEI concentration (wt %) on TA_HPAN3b (post-treated with GA for 60 minutes) and of **b)** GA post-treatment time (minutes) on TA_HPAN3b (PEI 1 wt %) performance. Screenings were performed using C_0 = 0.25 mg/mL of TsRTA for immobilization. Error bars represent the standard deviations obtained on triplicates.

Note: the effect of PEI concentration (wt %) on TsRTA leaching fraction (%) was not presented on graph **a)** since no significant differences were observed (due to the immobilized enzymes post-treatment with glutaraldehyde).

2.1.2 TA on PP membranes

Starting form the best system based on the PP membrane (TsRTA_PP3), the effects of PDA, GDE, and PEI functionalization times were studied (Figure S17). Increasing the dopamine polymerization time was found to have a significant impact on TA catalytic performance (Figure S17a). Low PDA functionalization times (i.e. 6 and 10 hours) resulted in membrane displaying higher enzyme leaching and poorer specific activity than those functionalized for 20 hours. The higher TA leaching might either be explained either by a poor anchoring of the resulting polydopamine layer to the PP surface due to incomplete polymerization (i.e. leaching of the TA_PDA_GDE_PEI layers), or by a different TA immobilization mechanism. The latter hypothesis is based on the fact that different chemical moieties (primary and secondary amines, quinones, catechols, etc) might be present at the PDA coating surface, depending on the dopamine polymerization state (Figure S18) [8]. Among all the reactive species generated, amines (I or II) will always be present in similar amounts, allowing the epoxy groups of GDE to be grafted onto the surface. However, there is a possibility that the TAs preferentially immobilize on other moieties (than epoxy) present at the carrier surface, such as quinones (covalent grafting) or catechols (electrostatic adsorption). Yet, this hypothesis is hard to prove due to the fact that the accurate structure and composition of PDA coatings is still questionable (despite being intensely characterized) [9]. On the contrary, the GDE grafting time (Figure S17b) did not affect the immobilization and catalytic performance of the biocatalysts, which suggests that the epoxy coupling is already be completed in 2 hours. Finally, PEI derivatization times higher than 90 minutes seem to enhance the TA leaching. This can be explained by the fact that, when using longer PEI derivatization times, a higher fraction of epoxy groups of GDE will be consumed by reaction with the amines groups of PEI. Thus, in the subsequent step of TA immobilization, the enzyme will have a lower chance to form stable covalent bonds by reactions with epoxy groups and instead mostly immobilize through (more labile) electrostatic adsorption. Thus, the TA electrostatic immobilization increases at the expense of the TA covalent grafting. Thus, the selected formulation of such catalyst seems to be achieved with 20 hours of PDA, 2 (or 18) hours of GDE, and 90 minutes of PEI.

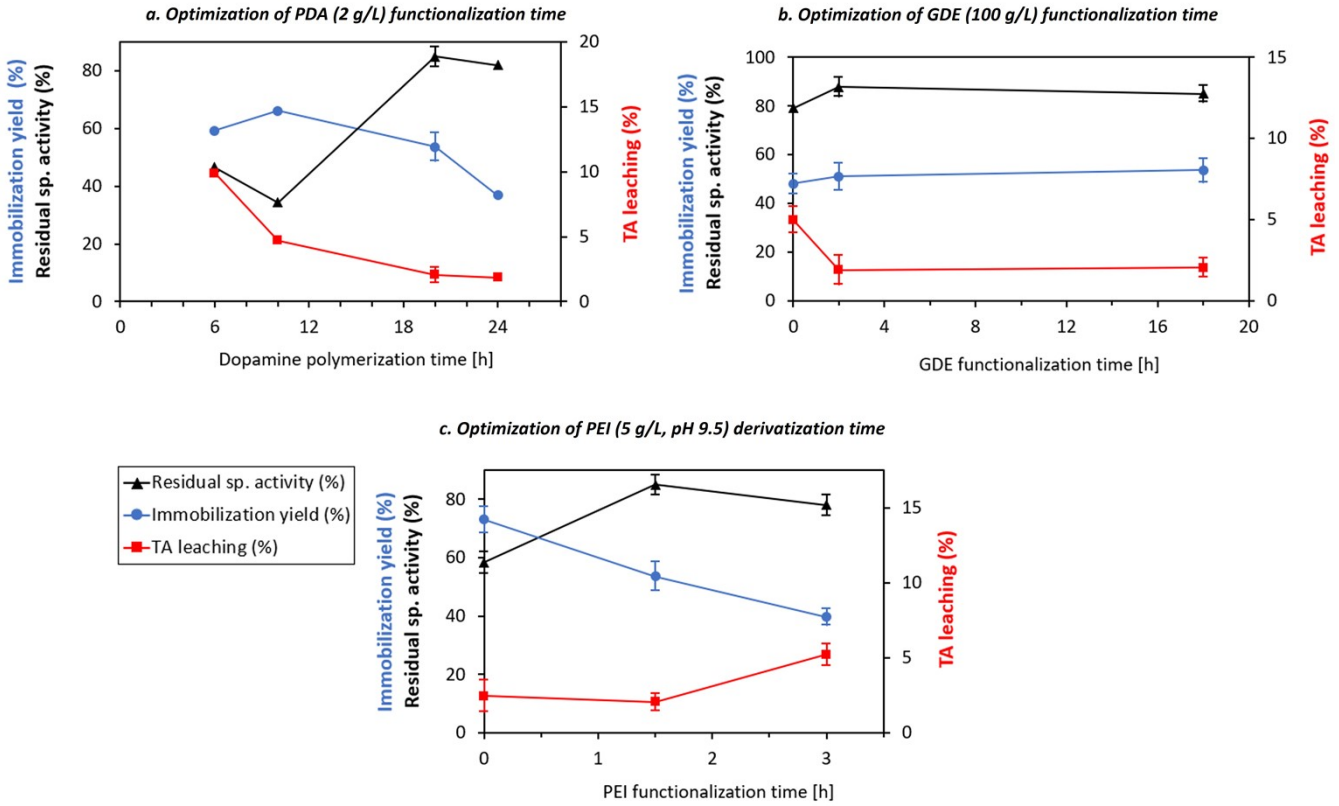

Figure S18. Impact of **a)** the PDA functionalization time on TA_PP3 (functionalized with GDE (18 hours) and PEI (1.5 hours)) ; **b)** the GDE functionalization time on TA_PP3 (functionalized with PDA (20 hours) and PEI (1.5 hours)) and **c)** the PEI functionalization time on TA_PP3 (functionalized with PDA (20 hours) and GDE (18 hours))**)** performance. Screenings were performed using C_0 = 0.25 mg/mL of TsRTA for immobilization. Error bars represent the standard deviations obtained on triplicates.

a.

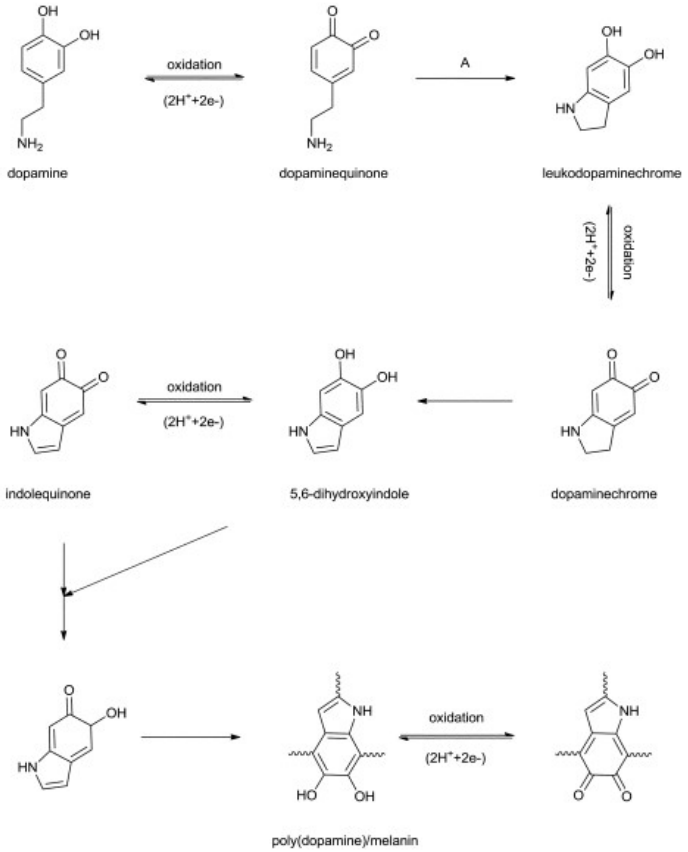

b.

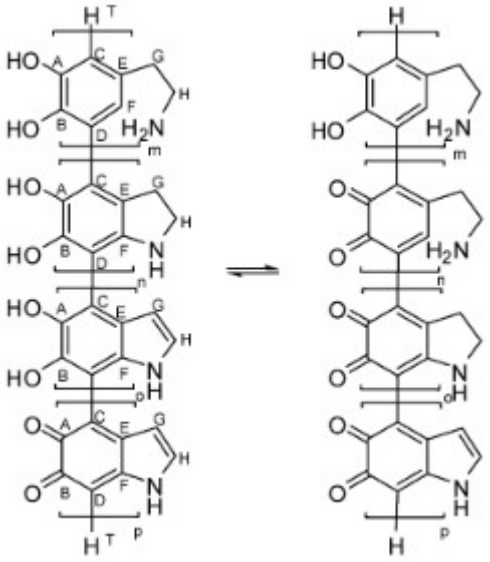

Figure S19 a. Representation of one possible dopamine polymerization mechanism, reprinted from Kamperman et al. (2014) [10]**, b.** Actual structure of PDA (obtained from 2 g/L dopamine hydrochloride in 10 mM Tris buffer pH 8.5, by air oxidation) proposed by Liebscher et al. (2013)[9].

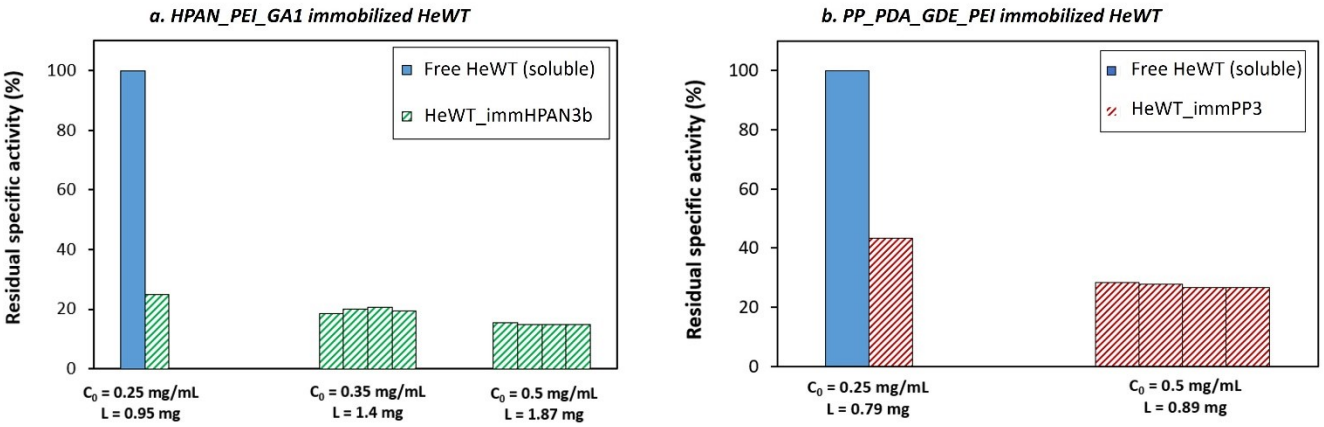

Figure S120. Reusability tests performed with **a)** HeWT_HPAN3b and **b)** HeWT_PP3 at different enzyme loadings (L). Each bar shown in **a)** and **b)** represent the residual specific activity (with respect to free HeWT), measured at each catalytic cycle (computed after 15 minutes).

Table S3. Summary of the catalytic performance displayed by the membrane-immobilized self-sufficient catalysts obtained, using TsRTA as transaminase.

Heterogeneous biocatalyst	Number of immob. steps	[PLP] for TA immob. [mM]	L_{PLP} [µmol]	TA imm. yield (%)	Activity [µmol.min^{-1}]	Sp. activity [µmol.min^{-1}.mg$_{TA}^{-1}$] **(recovery, in %)**
TA_PP3	1	1	0.46	39	0.55	0.54 **(74)**
TA_PP3_SS1	2	1	0.85	30	0.42	0.59 **(78)**
TA_PP3_SS0.1	2	0.1	0.97	84	0.63	0.28 **(41)**

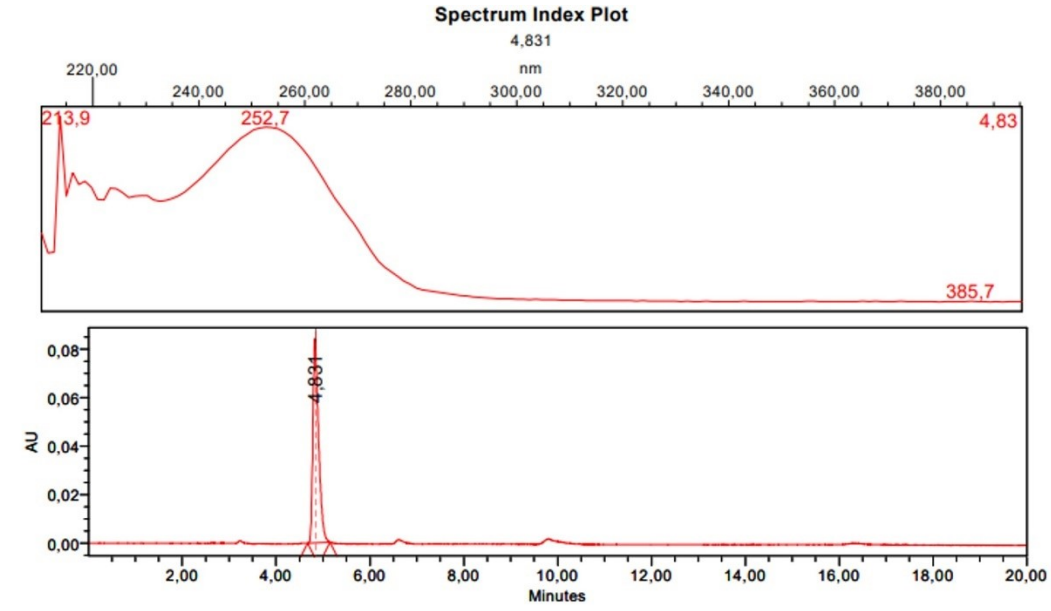

Peak Results

	Name	RT	Area	% Area
1		4,831	705943	100,00

Figure S21. Chiral HPLC chromatogram obtained by analyzing the BMBA produced after kinetic resolution, using TsRTA_PP_PDA_GDE_PEI.

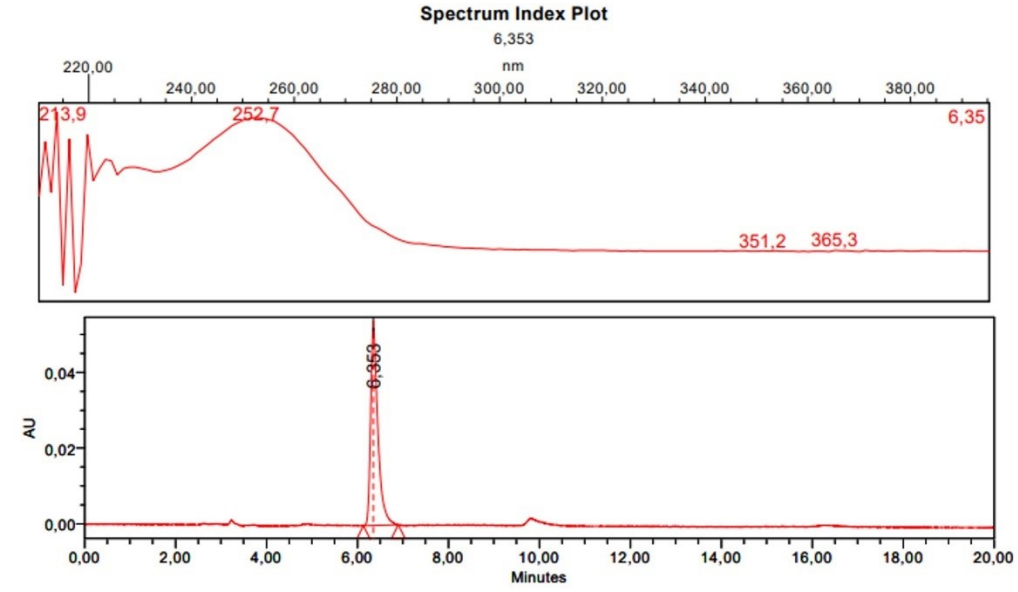

Peak Results

	Name	RT	Area	% Area
1		6,353	586111	100,00

Figure S22. Chiral HPLC chromatogram obtained by analyzing the BMBA produced after kinetic resolution, using HeWT_PP_PDA_GDE_PEI.

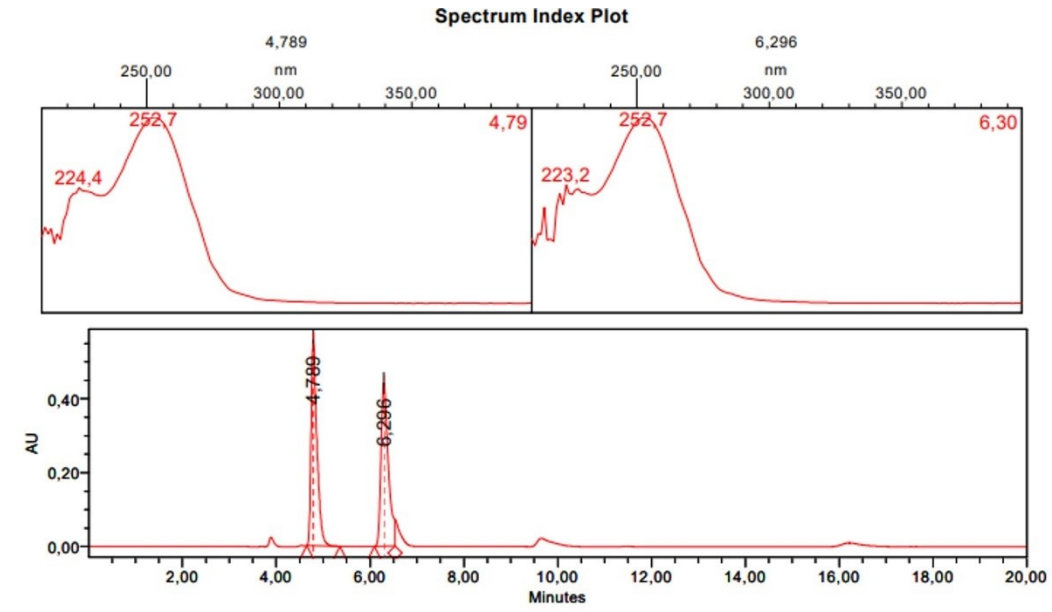

Peak Results

	Name	RT	Area	% Area
1		4,789	4788968	50,02
2		6,296	4785771	49,98

Figure S23. Chiral HPLC chromatogram obtained by analyzing commercial racemic BMBA product.

3 E-factor estimation

In this work, a kinetic resolution is used as a model reaction to demonstrate the effectiveness of the biocatalytic reaction with immobilized TA. The reaction is limited to 50% of yield. Hence, its E-factor will be penalized as compared to classical asymmetric synthesis of chiral amines (theoretical yield of 100%). Additionally, the most important advantage brought by the use of TA is indeed the enantioselectivity, which facilitates subsequent purification. Thus, a fully informative comparison of E-factor should also include the crucial purification steps.

Nevertheless, rough E-factor estimations for our batch transamination processes can be compared to benchmark processes (see Excel file added as supplementary file). Three common chemo-catalytic processes (methods A,B,C) for the synthesis of such enantiopure amines (i.e. α-methylbenzylamine derivatives) [11] have been used as benchmarks:

A. Imine asymmetric reductive amination (Figure S24) [12]: MBA (2a)

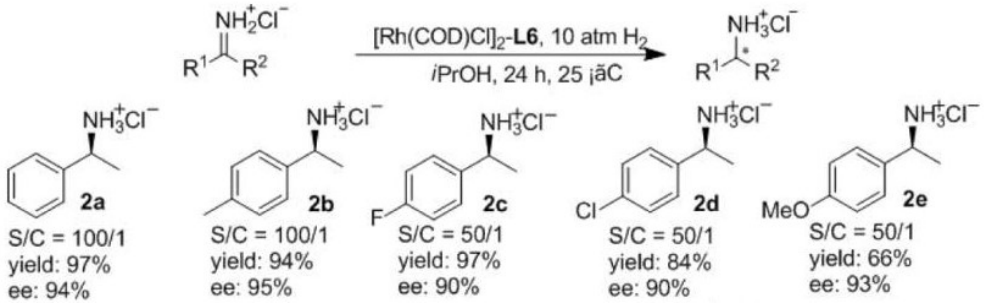

Figure S24. Imine asymmetric reductive amination as proposed by Zhang et al. (2014).

Protocol[12]: In nitrogen-filled glovebox, a solution of L6 (1.1 eqv.) and $[Rh(COD)Cl]_2$ (3.0 mg, 0.006 mmol) in 6.0 mL anhydrous i-PrOH was stirred at room temperature for 30 min. A specified amount of the resulting solution (2 mL) was transferred to a vial charged with 1a (0.2 mmol) by syringe. The vials were transferred to an autoclave, which was then charged with 10 atm of H_2 and stirred at 25 °C for 24 h.

B. Asymmetric reductive amination of keto-substrates (Figure S25) [13]**:** α-BMBA (6m)

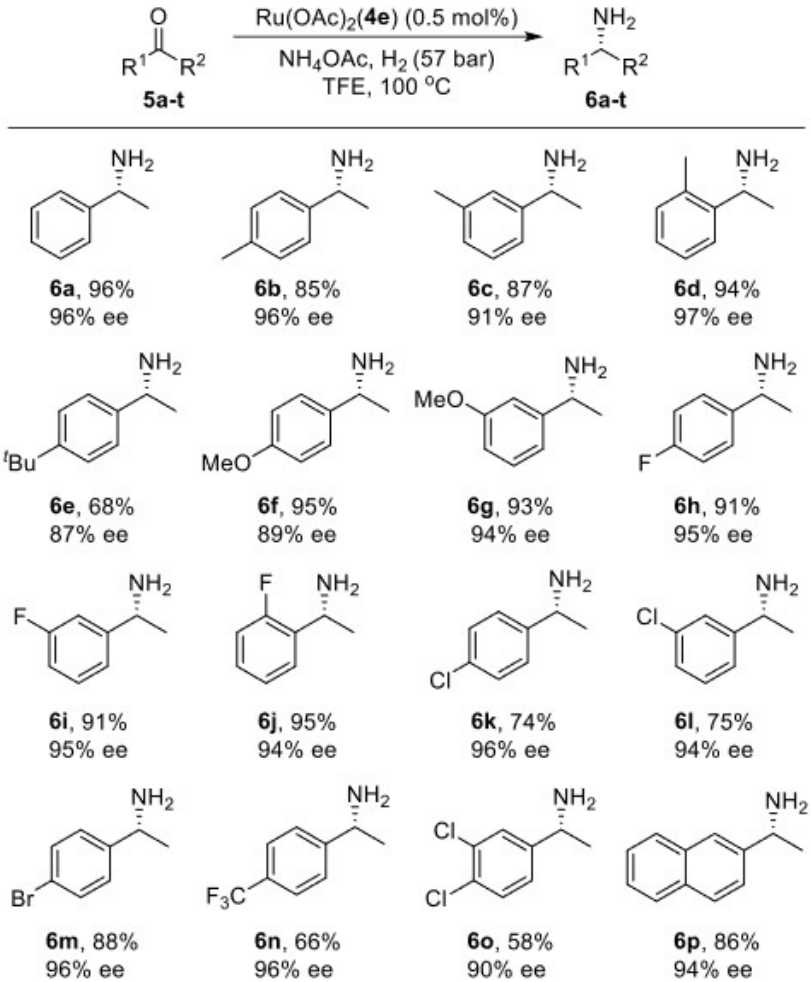

Figure S25. Ketone asymmetric reductive amination as proposed by Yin et al. (2018).

Protocol[13]: In a glovebox, required amount of the catalyst (0.5 mol %), substrate (0.2 mmol), ammonium salt (NH_4OAc, 0.4 mmol) and solvent (TFE = trifluoroethanol, 0.4 mL) were successively added to a vial equipped with a magnetic stirring bar. The mixture was then transferred to a stain-less autoclave and purged by three cycles of pressurization/venting with H_2. The required H_2 pressure was then installed and the autoclave was placed in an oil bath preheated to the indicated temperature. The autoclave was cooled down in an ice bath after the indicated reaction time and the pressure was slowly released.

C. Solvent switch-assisted chiral resolution of racemates (Figure S26) using a resolving agent [14]: MBA-TPA crystal salts.

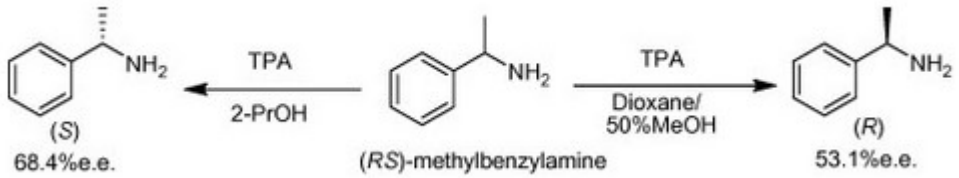

Figure S26. Solvent switch-assisted chiral resolution of racemates (Figure S26) using a resolving agent as described by Hirose et al. (2008).

Protocol[14]**:** A mixture of (RS)-MBA (121 mg, 1.0 mmol), N-tosyl-(S)-phenylalanine (S-TPA, 319 mg, 1.0 mmol), and the solvent (2-PrOH, using a 2-PrOH/(RS)-MBA ratio of 35 (v/w)) was heated to produce a clear solution. The solution was then cooled to room temperature to grow less-soluble salt crystals. The crystals were filtered off and washed with the respective solvent to afford the crude and less-soluble diastereomeric salt (S)-MBA:(S)-TPA. Yield (calculated based on half the amount of (RS)-MBA) and enantiomeric purity were of 69.8%. NB: please note that here, the resulting enantiopure amine is in the form of a crystal salt of S-MBA:S-TPA. No purification steps are indicated by the authors to obtain the enantiopure S-MBA.

E-factor were calculated through the following formula (Eq. (b)), and results are reported in Table S4.

$$E\,factor = \frac{\sum kg\ waste}{\sum kg\ target\ product} = \frac{\sum kg(unreacted\ reactants + by\ prod}{\sum kg\ target\ enantiop}$$

In these calculations:

- Water was not considered as a waste in the processes, hence its contribution was not taken into account into E-factor calculation.

- The contribution of H_2 gas (i.e. reactant in excess in benchmark processes A and B) was also neglected, due to the lack of information in the reported studies (this omission drives the E-factor of chemo-catalytic reactions lower)
- The mass of catalyst in our process is considered as zero, considering the complete recyclability of the membrane-immobilized TA (as opposed to homogeneous chemo-catalysts which are lost in each batch)
- Such metrics only cover the environmental performance **of the reactions**; the subsequent purification steps were not included in the E-factor calculation.

Table S4: Comparison of environmental performance (E-factor) of our biocatalytic transamination processes (D,E) with different benchmark chemocatalytic processes able to produce chiral amines.

Method	**A**	**B**	**C**	**D**	**E**
Description	Red. Amination	Red. Amination	Ch. resolution	Transamination	Transamination
Precursors	Imine, H_2	Ketone, H_2, NH_4OAc	Racemic amine	Ketone, pyr.	Ketone, pyr.
Catalyst	[Rh(COD)Cl]$_2$-(Ligand)	$Ru(OAc)_2$-(Ligand)	/ (use of a resolving agent)	TA_PP3_SS	TA free, PLP
ee (%)	90	95	69	99.9	99.9
E-factor	58	18	19	31 (17)*	32 (18)*

*: if HEPES 0.05 M was used instead of HEPES 0.1 M

We observe that E-factor values of model transamination (kinetic resolution) processes considered in this work are in the same range as the benchmark chemo-catalytic processes. However, it is noteworthy that our biocatalytic strategy produces enantiopure (B)MBA product, which is not the case of the other methods. Further purifications (e.g. preferential crystallizations, catalyst removal, chiral chromatography) will be required in the chemo-catalytic processes, which will markedly increase the overall E-factor of such chemo-catalytic processes. Purification is known to be a major driver for the overall (environmental) cost of the process of chiral amine synthesis [15,16]. This is the step of the process where the advantages of the membrane-biocatalyst will be plainly revealed. Unfortunately, we are not in the position to make such calculations that include the purification steps (due to lack of reported information on the complete chemo-catalytic processes).

4 Bibliography

1 M. M. Bradford, *Anal. Biochem.*, 1976, **72**, 248–254.

2 S. Gámez, E. de la Torre and E. M. Gaigneaux, *Chem. Eng. J.*, 2022, **427**, 131820.

3 C. M. Heckmann, B. Dominguez and F. Paradisi, *ACS Sustain. Chem. Eng.*, 2021, **9**, 4122–4129.

4 U. Montanari, D. Cocchi, T. M. Brugo, A. Pollicino, V. Taresco, M. Romero Fernandez, J. C. Moore, D. Sagnelli, F. Paradisi, A. Zucchelli, S. M. Howdle and C. Gualandi, *Polymers*, 2021, **13**, 1804.

5 J. M. Carceller, K. S. Arias, M. J. Climent, S. Iborra and A. Corma, *Natl. Sci. Rev.*, 2022, **9**, nwac135.

6 A. I. Benítez-Mateos, S. Bertella, J. Behaghel de Bueren, J. S. Luterbacher and F. Paradisi, *ChemSusChem*, 2021, **14**, 3198–3207.

7 M. Planchestainer, M. L. Contente, J. Cassidy, F. Molinari, L. Tamborini and F. Paradisi, *Green Chem.*, 2017, **19**, 372–375.

8 Y. Liu, K. Ai and L. Lu, *Chem. Rev.*, 2014, **114**, 5057–5115.

9 J. Liebscher, R. Mrówczyński, H. A. Scheidt, C. Filip, N. D. Hădade, R. Turcu, A. Bende and S. Beck, *Langmuir*, 2013, **29**, 10539–10548.

10 J. Yang, M. A. C. Stuart and M. Kamperman, *Chem. Soc. Rev.*, 2014, **43**, 8271–8298.

11 Q. Yin, Y. Shi, J. Wang and X. Zhang, *Chem. Soc. Rev.*, 2020, **49**, 6141–6153.

12 Q. Zhao, J. Wen, R. Tan, K. Huang, P. Metola, R. Wang, E. V. Anslyn and X. Zhang, *Angew. Chem. Int. Ed Engl.*, 2014, **53**, 8467–8470.

13 X. Tan, S. Gao, W. Zeng, S. Xin, Q. Yin and X. Zhang, *J. Am. Chem. Soc.*, 2018, **140**, 2024–2027.

14 T. Hirose, M. Begum, Md. Sadequl Islam, K. Taniguchi and M. Yasutake, *Tetrahedron Asymmetry*, 2008, **19**, 1641–1646.

15 C. K. Savile, J. M. Janey, E. C. Mundorff, J. C. Moore, S. Tam, W. R. Jarvis, J. C. Colbeck, A. Krebber, F. J. Fleitz, J. Brands, P. N. Devine, G. W. Huisman and G. J. Hughes, *Science*, 2010, **329**, 305–309.

16 J. Yang, A. Buekenhoudt, M. V. Dael, P. Luis, Y. Satyawali, R. Malina and S. Lizin, *Org. Process Res. Dev.*, 2022, **26**, 2052–2066.